Materials Advances

ROYAL SOCIETY OF CHEMISTRY

PAPER

View Article Online
View Journal

Cite this: DOI: 10.1039/d6ma00010j

Effects of anionic co-ligands and metal salts on the synthesis, solid-state structure and biological properties of mercury(II) complexes based on phosphorus ylide ligands

Sepideh Samiee, *[a] Habib Rashedi,[a] Valiollah Nobakht, †[ab] Hossein Motamedi,[c] Robert W. Gable [d] and Jan Janczak [e]

Six new dimeric and polymeric mercury(II) complexes with compositions of $[LHg(N_3)(\mu\text{-}Cl)]_2$ (**1**), $[LHg(Br)(\mu\text{-}Br)]_2$ (**2**), $[LHg(I)(\mu\text{-}I)]_2$ (**3**), $[LHg(SCN)(\mu\text{-}Cl)]_2$ (**4a**), $[LHg(SCN)(\mu\text{-}SCN)]_2$ (**4b**) and $[LHg(N_3)(\mu\text{-}N_3)]_n$ (**5**) (L = (4-bromobenzoyl)(triphenylphosphonio)methanide) have been synthesized and characterized using single-crystal X-ray diffraction, elemental analysis, and FT-IR and NMR spectroscopic studies. The reaction of mercury(II) chloride with L and excess sodium azide in methanol yields a dimeric chloride-bridged mercury–azide complex (**1**). In contrast, mercury(II) bromide and iodide form dimeric halide-bridged complexes (**2** and **3**), while mercury(II) acetate produces a polymeric mercury–azide complex (**5**). Dimeric mercury–thiocyanide complexes (**4a** and **4b**) are synthesized similarly to complex **1**, substituting KSCN for NaN_3. The results indicate that, under identical reaction conditions, azide anions act as terminal ligands, while thiocyanate functions as both bridging and terminal ligands, demonstrating that the final structures of mercury(II) complexes of phosphorus ylides are influenced by the mercury(II) salts and pseudohalide co-ligands used. Furthermore, the biological features of the synthesized mercury(II) complexes and the influence of pseudohalide ions (N_3^- and SCN^-) on these features are discussed.

Received 4th January 2026,
Accepted 14th May 2026

DOI: 10.1039/d6ma00010j

rsc.li/materials-advances

1. Introduction

The design and synthesis of transition metal polynuclear and polymeric complexes containing triatomic pseudohalide ligands such as thiocyanate (SCN^-), azide (N_3^-), and cyanate (NCO^-) have attracted considerable attention in coordination chemistry.[1–6] The unique ability of triatomic pseudohalide ions to stabilize the different oxidation states of transition metals increases the complexity and versatility of the resulting complexes.[7,8] Among these pseudohalides, azide ions are capable of adopting a number of coordination modes, including terminal and bridging configurations, which have a marked effect on the electronic and magnetic behaviour of the metal centers.[9–11] These properties make azido–metal complexes attractive for applications in materials science and molecular magnetism.[11] In a comparative context, thiocyanato–metal complexes, although less frequently studied,[12] exhibit intriguing properties that merit further investigation. The thiocyanate ion can participate in both terminal and bridging modes, displaying different geometries and coordination environments that can lead to unique electronic properties.[2,12–14] Preliminary studies have indicated that the presence of thiocyanate can alter the magnetic coupling between metal ions, potentially opening avenues for the development of new magnetic materials tailored for specific functionalities. Some bonding modes of these ions are illustrated in Fig. 1. Besides pseudohalide ligands, halide ions significantly influence the structural chemistry of transition-metal complexes because of differences in ionic radius and polarizability.[15] Larger, more polarizable halides (Br^- and I^-) increase the covalent character of metal–halide bonds, often distorting coordination geometries and stabilizing less common lattice motifs. In contrast, smaller, less polarizable halides (F^- and Cl^-) favor more ionic interactions, affording tighter, more symmetric coordination environments. These differences modify bond lengths, angles, and overall stability, and thus influence reactivity, solubility, and

[a] Department of Chemistry, Faculty of Science, Shahid Chamran University of Ahvaz, Ahvaz, Iran. E-mail: s.samiee@scu.ac.ir, samiee.sepideh@gmail.com; Fax: +98 6133337009; Tel: +98 6133331042
[b] Department of Chemistry, College of Science, Shiraz University, 7194684795 Shiraz, Iran
[c] Department of Biology, Faculty of Science, and Biorefinery Research Center, Shahid Chamran University of Ahvaz, Ahvaz, Iran
[d] School of Chemistry, University of Melbourne, Victoria 3010, Australia
[e] Institute of Low Temperature and Structure Research, Polish Academy of Sciences, Okólna 2 str., 50-422 Wroclaw, Poland
† Present address: Department of Chemistry, College of Science, Shiraz University, 7194684795 Shiraz, Iran.

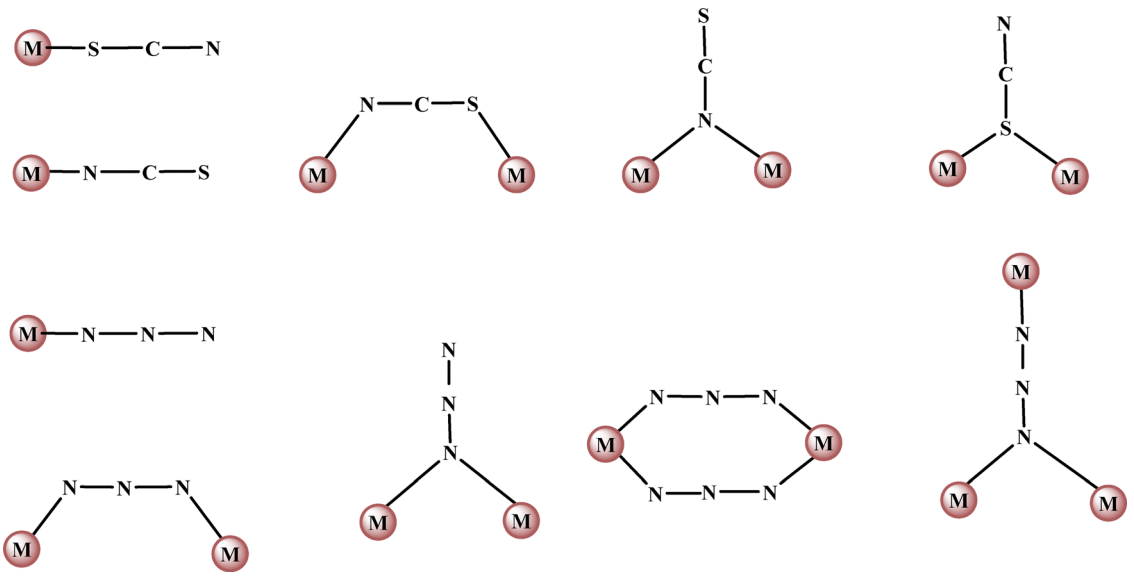

Fig. 1 Some bonding modes of thiocyanate and azide anions.

electronic properties.[16] Thus, the halide identity can also govern the crystal packing and topology in extended metal–organic polymers.

The coordination chemistry of ylides has also emerged as an important area of research in organometallic and coordination chemistry.[17] Among them, α-keto-stabilized phosphorus ylides are well known as appropriate ligands due to their high stability and ambidentate properties.[18–20] Phosphorus ylides of the type $R_3P{=}C(H)C(O)R$ coordinate to metal ions *via* either the carbanion (C-coordination) or the enolate oxygen (O-coordination). Soft metal ions prefer the ylidic carbon, while hard metal ions interact with the carbonyl oxygen.[21,22] Nesmeyanov and coworkers[23] first synthesized complexes of phosphorus ylides and mercury(II) halides in 1965. Later, Kalyanasundari *et al.* confirmed an asymmetric halide-bridged dimeric structure for these complexes in 1995 using single-crystal X-ray diffraction.[24] To date, numerous mercury(II) complexes derived from phosphorus ylides have been reported, typically exhibiting mononuclear or halide-bridged dimeric structures.[25–27] Notably, pseudohalide ligands such as azide and thiocyanate exhibit rich coordination flexibility, including terminal, bridging, and polydentate binding modes, which can significantly influence the overall structural topology. Despite this potential, their integration into mercury(II) complexes of phosphorus ylides is rarely reported in the literature. A search of the Cambridge Structural Database[28] found many Hg–halide structures, of which there are 929 structures with the $[Hg_2X_2]^{2+}$ core. There are 422 mercury thiocyanate structures, 88 with the thiocyanate bridging two Hg atoms, one with S-bonded monodentate coordination, and two structures with end-on S-bridging between two mercury atoms. There is only one structure with an N-bonded thiocyanate, $[Hg(NCS)_4]$.[29] In contrast, there are 33 mercury structures with a monodentate azide, 11 with end-on-bridging azides and 2 with end-to-end bridging azides. There were only 13 organomercury azide structures and 2 organomercury thiocyanate structures. This indicates that while a number of different structures are possible, depending on the mercury halide and the ligand used, mercury halide structures dominate. Hence, the present study introduces distinct structures by combining pseudohalide co-ligands with mercury(II) halide complexes of phosphorus ylide, which have not been observed in previously reported Hg–ylide or Hg–pseudohalide complexes.[30–34]

In recent years, metal complexes incorporating stabilized phosphorus ylides have attracted attention due to their diverse biological properties, arising from the ability of the metal center to interact with biologically relevant donor atoms and disrupt essential cellular processes. In this context, mercury(II) complexes are of particular interest.[19,27,33,35,36] As a soft Lewis acid, Hg(II) exhibits strong affinity toward sulfur- and nitrogen-containing biomolecular sites (*e.g.*, thiol groups in enzymes), leading to enzyme inhibition and disruption of cellular redox balance, which underlies its antibacterial activity.[37–39] Despite concerns regarding mercury toxicity, its application in controlled antibacterial systems remains relevant.[40–42] Recent studies have shown that appropriate ligand design, particularly using strongly coordinating ligands such as phosphorus ylides, can significantly enhance the stability and kinetic inertness of Hg(II) complexes, thereby limiting the release of free Hg(II) ions and reducing nonspecific toxicity.[40–42] In this regard, ylide-based ligand frameworks also enable the modulation of lipophilicity and cellular uptake, providing a strategy to balance biological activity and safety. Accordingly, mercury(II) complexes containing phosphorus ylides offer a suitable platform for investigating structure–activity relationships in antibacterial systems.

As a continuation of our recent work,[43] we report novel azido- and thiocyanato–mercury(II) complexes containing phosphorus ylides and examine the influence of coligands (N_3^- and SCN^-) and mercury(II) salts (HgX_2 and $Hg(OAc)_2$) on the

synthesis, molecular structures, and biological properties of these complexes.

2. Experimental

2.1. Materials and physical measurements

All reagents and solvents were purchased commercially and used as received. Microanalyses were performed using a Heraeus CHN-O-Rapid analyzer. The infrared spectra (4000–400 cm^{-1}) were recorded on a PerkinElmer spectrophotometer using KBr pellets. The ^{31}P, ^{1}H and ^{13}C NMR spectra were recorded in a $CDCl_3$ solution at 25 °C on a 250-MHz Bruker spectrometer. Chemical shifts (ppm) were reported according to the internal standard H_3PO_4 (85%) for ^{31}P NMR spectroscopy and TMS for ^{1}H and ^{13}C NMR spectroscopies. Melting points were measured on an SMP3 apparatus. X-ray powder diffraction patterns were recorded on a Philips X'Pert Pro diffractometer (CuKα radiation, λ = 1.54184 Å) within the 2θ range of 5°–50°. Structural analyses were performed using the Mercury[44] and TopospPro[45] software packages.

2.2. Synthesis

Manipulations were performed under dry N_2 using standard Schlenk techniques unless stated otherwise. All the reagents were purchased from commercial sources and used as received without any purification. The phosphorus ylide ligand, $Ph_3PC(H)C(O)C_6H_4$-*p*-Br (**L**), was synthesized as per the procedure reported by Sabounchei and coworkers.[20]

2.2.1. Synthesis of the dimeric mercury–azide complex (1). Sodium azide (0.6 mmol, 0.04 g) in 5 mL of methanol was added dropwise to a stirred mixture of mercury(II) chloride (0.2 mmol, 0.054 g) and **L** (0.2 mmol, 0.1 g) in 6 mL of methanol at room temperature. The mixture was then stirred for 24 h at 40–50 °C. After filtering the resulting colourless solution, it was left undisturbed for several days, leading to the formation of needle-shaped colourless crystals through slow evaporation. Yield: 0.06 g, 90%; m.p. 191–193 °C. Anal. calc. for $C_{52}H_{40}Br_2Cl_2Hg_2N_6O_2P_2$: C, 42.35%; H, 2.73%; N, 5.70%. Found: C, 42.05%; H, 2.45%; N, 5.56%. IR (KBr disk): ν(C═O) 1636 cm^{-1}, ν(P–C) 814 cm^{-1}, $\nu(N_3)$ 2044 cm^{-1}. ^{31}P NMR (DMSO-d_6): 17.93 (s). ^{1}H NMR (DMSO-d_6): 4.97 (db, 1H, CH); 7.56–7.89 (m, 16H, Ph). $^{13}C\{^{1}H\}$ NMR (DMSO-d_6): 46.32 (d, CH, $^{2}J_{PC}$ = 100.01 Hz); 117.57–130.47 (m, Ph); 186.08 (s, CO).

2.2.2. Synthesis of the dimeric mercury–halide complexes (2 and 3). A similar synthetic procedure to that used for **1** was used for **2** and **3**, except that $HgCl_2$ was replaced by $HgBr_2$ (0.2 mmol, 0.07 g) or HgI_2 (0.2 mmol, 0.1 g), respectively. All attempts to synthesize new complexes from the two mercury halides in the presence of sodium azide were unsuccessful. The known halide-bridged dimeric complexes $[LHg(Br)(\mu\text{-}Br)]_2$ (**2**) and $[LHg(I)(\mu\text{-}I)]_2$ (**3**) were obtained with their spectroscopic properties identical to those previously reported.[20] Colourless needle-like single crystals of complex **3**, suitable for crystal structural analysis, were formed by slow evaporation from methanol.

Data for complex 2. Yield: 0.07 g, 85%; m.p. 200–202 °C. Anal. calc. for $C_{26}H_{20}OPHgBr_3$: C, 38.10%; H, 2.46%. Found: C, 38.25%; H, 2.40%. IR (KBr disk): ν(C═O) 1632 cm^{-1}, ν(P–C) 807 cm^{-1}. ^{31}P NMR ($CDCl_3$): 20.37 (s). ^{1}H NMR ($CDCl_3$): 5.25 (br, 1H, CH); 7.55–8.25 (m, 16H, Ph). $^{13}C\{^{1}H\}$ NMR ($CDCl_3$): 50.74 (br); 120.297–130.34 (m, Ph); 182.84 (s, CO).

Data for complex 3. Yield: 0.06 g, 82%; m.p. 195–197 °C. Anal. calc. for $C_{26}H_{20}OPBrHgI_2$: C, 34.17%; H, 2.21%. Found: C, 34.08%; H, 2.27%. IR (KBr disk): ν(C═O) 1625 cm^{-1}, ν(P–C) 808 cm^{-1}. ^{31}P NMR ($CDCl_3$): 18.20 (s). ^{1}H NMR ($CDCl_3$): 5.18 (br, 1H, CH); 6.24–7.78 (m, 16H, Ph). $^{13}C\{^{1}H\}$ NMR ($CDCl_3$): 50.50 (bd); 119.55–138.00 (m, Ph); 189.37 (s, CO).

2.2.3. Synthesis of the dimeric mercury–thiocyanide complex (4). This complex was synthesized following a similar procedure used for the synthesis of complex **1**, except that potassium thiocyanate (0.8 mmol, 0.08 g) was used as a co-ligand instead of sodium azide. Yield: 0.06 g, 85%; m.p. 155–158 °C. IR (KBr disk): ν(C═O) 1688 cm^{-1}, ν(P–C) 771 cm^{-1}, ν(SCN, N-coordinated) 2117 cm^{-1}, ν(SCN, S-coordinated) 2065 cm^{-1}. $^{31}P\{^{1}H\}$ NMR ($CDCl_3$): 21.92 (s); 23.75 (s). ^{1}H NMR ($CDCl_3$): 4.80 (br, 1H, CH); 7.48–833 (m, 16H, Ph). $^{13}C\{^{1}H\}$ NMR ($CDCl_3$): 53.75 (br, CH); 117.86–147.33 (m, Ph); 181.75 (CO).

2.2.4. Synthesis of the polymeric mercury–azide complex (5). This complex was synthesized following a similar procedure used for the synthesis of complex **1**, except that mercury(II) acetate (0.2 mmol, 0.07 g) was used as a metal salt instead of mercury(II) chloride. Yield: 0.056 g, 80%; m.p. 192–195 °C. Anal. calc. for $C_{26}H_{20}BrHgN_6O$: C, 42.35%; H, 2.73%; N, 5.70%. Found. C, 41.87%; H, 2.45%; N, 5.56%. IR (KBr disk): ν(C═O) 1644 cm^{-1}, ν(P–C) 831 cm^{-1}, $\nu(N_3$, terminal) 2046 cm^{-1}, $\nu(N_3$, bridging) 1998 cm^{-1}. $^{31}P\{^{1}H\}$ NMR ($CDCl_3$): 20.26 (s). ^{1}H NMR ($CDCl_3$): 4.85 (br, CH); 7.51–7.71 (m, 16H, Ph). $^{13}C\{^{1}H\}$ NMR ($CDCl_3$): 62.82 (d, CH, $^{1}J_{PC}$ = 108.82 Hz); 123.32–133.46 (m, Ph); 183.35 (CO).

2.3. Determination of X-ray crystallographic structures

Colourless single crystals of complexes **1**, **3**, **4a** and **4b** and **5** were crystallized by slow evaporation from methanol; the crystals of **4a** and **4b** were obtained from the same solution. Many crystals of **3** were disordered; the crystal selected showed relatively minor disorder. Data collections for **1**, **4a** and **4b** were carried out on an XtaLab Synergy diffractometer using mirror monochromated Cu Kα radiation (λ = 1.54184 Å) at 100 K. Gaussian absorption corrections were applied to the data for all three crystals.[46] Data for **5** and **3** were collected at 100 K at the MX2 beamline at the Australian Synchrotron, fitted with a silicon double-crystal monochromator and a Dectris EIGER 16M detector, with the wavelength tuned to approximate Mo-Kα radiation (λ = 0.710917 Å).[47] Data reduction was performed with XDS[48] using multi-scan absorption corrections using SADABS.[49] Using Olex2,[50] the structures were solved with the ShelXT[51] structure solution program using intrinsic phasing and refined with the ShelXL[52] refinement package using least squares minimization on F^2, using all data. All non-hydrogen atoms were refined with anisotropic displacement parameters,

Table 1 Crystallographic data and processing parameters of the studied complexes

Compound	1	3	4a	4b	5
Empirical formula	$C_{52}H_{40}Br_2Cl_2Hg_2N_6O_2P_2$	$C_{52}H_{40}Br_2Hg_2I_4O_2P_2$	$C_{54}H_{40}Br_2Cl_2Hg_2N_2O_2P_2S_2$	$C_{56}H_{40}Br_2Hg_2N_4O_2P_2S_4$	$C_{26}H_{20}BrHgN_6OP$
Formula weight	1474.74	1827.38	1506.84	1552.10	743.95
Temperature/K	100.00(10)	100(2)	99.98(11)	100.01(10)	100(2)
Crystal system	Monoclinic	Triclinic	Monoclinic	Orthorhombic	Tetragonal
Space group	$P2_1/c$	$P\bar{1}$	$P2_1/c$	$Pbca$	$P\bar{4}2_1c$
a/Å	12.29610(10)	10.036(2)	12.47316(11)	21.39445(12)	24.068(3)
b/Å	19.8695(2)	11.977(2)	19.68409(13)	9.92513(6)	24.068(3)
c/Å	11.01480(10)	12.779(3)	11.48720(9)	25.51536(14)	8.5920(17)
α/°	90	72.25(3)	90	90	90
β/°	109.2390(10)	68.02(3)	110.2525(9)	90	90
γ/°	90	71.81(3)	90	90	90
Volume/Å^3	2540.81(4)	1322.0(6)	2646.00(4)	5418.00(5)	4977.1(17)
Z	2	1	2	4	8
ρ_{calc} g cm^{-3}	1.928	2.295	1.891	1.903	1.986
μ/mm^{-1}	14.467	9.745	14.604	14.116	7.888
F(000)	1408.0	840.0	1440.0	2976.0	2848.0
Crystal size/mm^3	0.314 × 0.133 × 0.086	0.05 × 0.02 × 0.02	0.176 × 0.107 × 0.063	0.221 × 0.045 × 0.021	0.08 × 0.02 × 0.02
Reflections collected	29 002	23 681	37 600	78 564	90 365
Data/restraints/parameters	5475/0/308	6845/0/290	5702/0/308	5886/0/325	8108/0/326
Goodness-of-fit on F^2	1.134	1.079	1.117	1.078	1.075
Final R indexes [$I \geq 2\sigma(I)$]	R_1 = 0.0296, wR_2 = 0.0685	R_1 = 0.0298, wR_2 = 0.0754	R_1 = 0.0245, wR_2 = 0.0620	R_1 = 0.0229, 0.0602	R_1 = 0.0252, wR_2 = 0.0601
Largest diff. peak/hole/e Å^{-3}	1.16/−0.82	2.48/−2.69	1.05/−0.77	0.81/−0.81	1.22/−1.12

while all hydrogen atoms were placed at geometrical estimates and refined using the riding model with an isotropic displacement parameter of 1.5U_{eq} of the parent atom for all methyl carbon atoms and 1.2U_{eq} of the parent atom for all other atoms. The maximum and minimum electron density peaks were close to the Hg and Br atoms; for all structures, except for **3**, peak heights were less than 1.25 e Å^{-3}. For complex **3**, the maximum and minimum peak heights were 2.48 and −2.69 e Å^{-3}, respectively, attributable to the crystal disorder; attempts to model this disorder were not successful. A summary of the crystallographic data and structure refinement details is given in Table 1, and the selected bond lengths and angles are listed in Table 2.

2.4. Biological studies

2.4.1. Antibacterial activity. In the bioassay of the prepared mercury(II) complexes **1–5**, the antibacterial activity of these compounds was assessed against two Gram-positive bacteria, *i.e.*, *Staphylococcus aureus* (ATCC 6538) and *Bacillus subtilis* (ATCC 6633), as well as two Gram-negative species, namely, *Escherichia coli* (ATCC 25922) and *Pseudomonas aeruginosa* (ATCC 9027). A fresh culture was prepared in Mueller-Hinton broth (Merck, Germany) from these species and incubated at 37 °C until its bacterial density reached 0.5 McFarland turbidity. Six different concentrations, namely, 200, 100, 50, 25, 12.5 and 6.25 μg mL^{-1}, of each compound were prepared in 1 mL of sterile Mueller-Hinton broth, and 100 μL of the bacterial suspension with 0.5 McFarland turbidity was added to the test tubes. All tubes were incubated at 37 °C with continuous shaking at 70 rpm for 24 h. A culture from each species was also prepared without any test compound and regarded as the growth positive control. Furthermore, non-inoculated culture media containing test compounds were regarded as the growth negative controls. Following incubation, the bacterial growth and turbidity were assessed in all tubes. Lack of turbidity was regarded as bacterial growth inhibition. The lowest concentration in the above series that inhibited bacterial growth was regarded as the minimum inhibitory concentration (MIC) index. A loopful from growth negative tubes was cultured on sterile Mueller-Hinton agar and incubated at 37 °C for 24 h. The lowest concentration that was able to inhibit bacterial growth and colony formation was reported as the minimum bactericidal concentration (MBC) index. Simultaneously, the effect of some reference antibiotics, including gentamicin, ceftriaxone, ceftizoxime, tetracycline, cephalexin, enrofloxacin, imipenem and cloxacillin, was evaluated against the target bacteria in a Kirby-Bauer disc diffusion antimicrobial susceptibility test, and the growth inhibition zone for each antibiotic was recorded.

2.4.2. Antifungal activity. The antifungal activity of the prepared compounds was investigated against *Aspergillus niger* (PTCC 5320) and *Aspergillus flavus* (PTCC 5006). These species were cultured on potato dextrose agar (PDA, Merck, Germany) for 72 h at 30 °C. Subsequently, a spore suspension equal to 0.5 McFarland turbidity was prepared from them in sterile physiological saline (0.9% NaCl). Two different concentrations, 0.5 and 1 mg mL^{-1}, of the synthesized compounds were prepared in sterile Mueller-Hinton broth and inoculated with 100 μL of the spore suspension. The tubes were incubated at 30 °C for 48 h, and the fungal growth was monitored. Lack of turbidity and fungal hyphae growth was regarded as antifungal activity. A loopful was then cultured on potato dextrose agar (PDA, Merck, Germany) and incubated at 30 °C for 48 h in order to find the fungicidal or fungistatic potential of compounds. Simultaneously, the effect of fluconazole, miconazole, itraconazole,

Table 2 Selected bond lengths (Å) and angles (°) for complexes **1**, **3**, **4a**, **4b** and **5**

	1	**3**		**4a**		**4b**		**5**	
Bond lengths									
Hg1–C1	2.175(4)	Hg1–C1	2.287(3)	Hg1–C1	2.198(3)	Hg1–C1	2.245(3)	Hg1–C1	2.141(4)
Hg1–Cl1	2.5980(9)	Hg1–I1	2.7926(10)	Hg1–Cl1	2.5164(7)	Hg1–S1	2.5014(7)	Hg1–N1	2.098(4)
Hg1–Cl1^a	2.7742(9)	Hg1–I1^a	3.1575(7)	Hg1–Cl1^a	2.7949(7)	Hg1–S2	2.5303(7)	Hg1–N4	2.488(4)
Hg1–N1	2.174(4)	Hg1–I2	2.6949(11)	Hg1–S1	2.4683(9)	Hg1–N2^a	2.533(2)	Hg1–N6^b	2.606(4)
N1–N2	1.195(5)			S1–C27	1.668(4)	S1–C27	1.674(3)	N1–N2	1.226(6)
N2–N3	1.147(5)			N1–C27	1.155(5)	S2–C28	1.662(3)	N2–N3	1.153(6)
						N1–C27	1.159(4)	N4–N5	1.189(6)
						N2–C28	1.159(4)	N5–N6	1.171(5)
Bond angles									
C1–Hg1–Cl1^a	100.72(10)	I1–Hg1–I1^a	92.19(3)	C1–Hg1–Cl1^a	99.19(8)	C1–Hg1–N2^a	96.86(9)	C1–Hg1–N4	106.51(14)
C1–Hg1–Cl1	117.85(10)	I2–Hg1–I1^a	100.72(2)	C1–Hg1–Cl1	120.38(8)	C1–Hg1–S1	125.10(7)	C1--Hg1–N6^b	96.55(14)
C1–Hg1–N1	145.35(14)	I2–Hg1–I1	114.83(3)	C1–Hg1–S1	134.71(8)	C1–Hg1–S2	126.51(7)	C1–Hg1–N1	161.47(16)
Cl1–Hg1–Cl1^a	88.62(3)	C1–Hg1–I1^a	95.51(8)	Cl1–Hg1–Cl1^a	90.54(2)	S1–Hg1–N2^a	104.28(6)	N1–Hg1–N4	89.67(14)
N1–Hg1–Cl1^a	92.16(10)	C1–Hg1–I1	116.14(8)	S1–Hg1–Cl1^a	92.84(3)	S2–Hg1–N2^a	88.68(5)	N1–Hg1–N6^b	91.70(15)
N1–Hg1–Cl1	94.27(10)	C1–Hg1–I2	125.46(8)	S1–Hg1–Cl1	102.85(3)	S1–Hg1–S2	104.33(2)	N4-Hg1- N6^b	92.16(13)
Hg1–Cl1–Hg1^a	91.38(3)	Hg1–I1–Hg1^a	87.81(3)	Hg1–Cl1–Hg1^a	89.46(2)				
N2–N1–Hg1	112.8(3)			C27–S1–Hg1	97.38(12)	C27–S1–Hg1	96.66(10)	N2–N1-Hg1	114.5(3)
N3–N2–N1	177.4(4)					C28–S2–Hg1	99.55(9)	N5–N4-Hg1	120.6(3)
						C28–N2–Hg1^a	143.7(2)	N5–N6-Hg1^c	118.0(3)
				N1–C27–S1	177.6(3)	N1–C27–S1	178.5(3)	N3–N2–N1	174.6(5)
						N2–C28–S2	177.5(3)	N6–N5–N4	178.2(5)
Torsion angles									
Hg1^a…Hg–N1–N2	−23.8(2)			Hg1^a…Hg–S1–C27	−32.26(11)				
C1–Hg1–N1–N2	−178.7(3)			C1–Hg1–S1–C27	179.99(16)	C1–Hg1–S1–C27	141.39(12)	C1–Hg1–N1–N2	11.8(7)
						C1–Hg1–S2–C28	63.05(13)	C1–Hg1–N4–N5	−48.0(4)
Cl1–Hg1–N1–N2	22.5(2)			Cl1–Hg1–S1–C27	17.11(12)	S1–Hg1–S2–C28	−138.92(10)	N1–Hg1–N4–N5	122.9(4)
						S2–Hg1–S1–C27	−17.05(10)	N4–Hg1–N1–N2	−139.4(4)
						N2^1–Hg1–S1–C27	−109.37(11)	N6^1–Hg1–N1–N2	128.4(4)
						N2^1–Hg1–S2–C28	−34.51(11)	N6^1–Hg1–N4–N5	−145.5(3)
Hg1–C1–C2–O1	−86.5(4)	Hg1–C1–C2–O1	−90.9(3)	Hg1–C1–C2–O1	−85.7(3)	Hg1–C1–C2–O1	−99.0(2)	Hg1–C1–C2–O1	−98.8(4)

^{a} $1-x, 1-y, 1-z$. ^{b} $1/2-y, 1/2-x, -1/2+z$. ^{c} $1/2-y, \frac{1}{2}-x, 1/2+z$.

amphotericin B and nystatin as standard antifungal antibiotics against target fungi was evaluated through the disc diffusion assay method.

3. Results and discussion

3.1. Synthesis of the dimeric and polymeric mercury(II) complexes

The chemical structures of the mercury complexes, together with their reaction paths, are presented in Scheme 1. The reactions of equimolar amounts of the methanolic solution of mercury(II) salts (HgX_2 or $Hg(CH_3COO)_2$) with a phosphorus ylide ligand, **L**, in the presence of excess anionic co-ligands (N_3^- or NCS^-) afford four categories of mercury complexes: the dimeric mercury–azide–halide complex (**1**), the dimeric mercury–halide complexes (**2** and **3**), a mixture of two dimeric mercury–thiocyanide complexes (**4a** and **4b**) and the polymeric mercury–azide complex (**5**). The precise structures of all complexes (except **2**) were determined using single-crystal X-ray crystallography, supported by spectroscopic characterization (FT-IR spectroscopy and ^{31}P, ^{1}H, ^{13}C NMR spectroscopies) and elemental analyses.

A closer inspection of Scheme 1 reveals that by tuning the mercury salts and pseudohalide co-ligands, novel mercury(II) complexes with phosphorus ylides can be obtained. In the presence of azide ions, a dimeric complex, $[LHg(N_3)(\mu\text{-}Cl)]_2$ (**1**), is formed with terminal azide ligands and bridging chlorine atoms, whereas in the presence of thiocyanate ions, two different dimeric mercury–thiocyanate complexes, $[LHg(SCN)(\mu\text{-}Cl)]_2$ (**4a**) and $[LHg(SCN)(\mu\text{-}SCN)]_2$ (**4b**), are formed. Different mercury salts can also give complexes with varying structures. Mercury chloride yields a dimeric complex with terminal azide ligands (**1**); using mercury bromide or iodide produces dimeric halide-bridged complexes, $[LHg(X)(\mu\text{-}X)]_2$ [X = Br (**2**) and I (**3**)], while using mercury acetate results in a polymeric azido-bridged complex $[LHg(N_3)(\mu\text{-}N_3)]_n$ (**5**). A comparison of the structure of compound **1** with that of compounds **3** and **5** highlights the influence of mercury salts on the structural characteristics of these compounds. In contrast, the comparison of compound **1** with compound **4** illustrates how typical pseudohalide co-ligands contribute to the structural diversity of mercury(II) complexes with phosphorus ylides. The failure to form azide complexes with $HgBr_2$ and HgI_2 is presumably due to the preference of mercury to form complexes with iodide or bromide rather than azide, forming only $[LHg(Br)(\mu\text{-}Br)]_2$ (**2**) and $[LHg(I)(\mu\text{-}I)]_2$ (**3**), respectively. Azide coordinates to mercury only in the presence of chloride, as a monodentate ligand, giving $[LHg(N_3)(\mu\text{-}Cl)]_2$ (**1**); nevertheless, the chloride-bridged

$[Hg(\mu\text{-}Cl)]_2$ moiety is preserved. With thiocyanate, two products are formed: $[LHg(SCN)(\mu\text{-}Cl)]_2$ (**4a**), in which SCN^- replaces the terminal azide, but the $[Hg(\mu\text{-}Cl)]_2$ core remains, and $[LHg(SCN)(\mu\text{-}SCN)]_2$ (**4b**), in which bridging thiocyanates fully replace chloride. This indicates that the preference of mercury for (bridging) thiocyanate and (bridging) chloride in this system is similar. An azide-only polymer, $[LHg(N_3)(\mu\text{-}N_3)]_n$ (**5**), is formed only when no halide is present in the reaction mixture. It seems that the difference in the reactivity of mercury(II) salts and anionic co-ligands can be explained by the hard-soft acid–base (HSAB) theory.[53,54] Mercury is a soft, highly polarizable acid and therefore prefers to bind soft bases.[55–57] The observed ligand preference appears to follow the order of $I^- > Br^- > SCN^- > Cl^- > N_3^-$. The resulting products may also be affected by the ability of thiocyanate and azide to act as bridging ligands between two metal centers.[58]

3.2. IR and NMR spectra of the mercury complexes

The structures of the products were successfully corroborated by Fourier transform infrared (FT-IR) and ^{31}P, ^{1}H and ^{13}C NMR spectroscopic methods (Fig. S1–S18 in the SI). In the IR spectra of all complexes, the increase in the frequency of the ν(CO) bands (around 1600 cm^{-1}) compared to **L** (free ligand) indicates that the mercury complexes are formed. As noted in the literature,[25–27] the coordination mode through ylidic carbon causes a significant increase in the ν(CO) frequency. In the IR spectrum of complex **1**, the narrow, intense band at 2044 cm^{-1} indicates the presence of terminal azide groups, while the strong double bands at 2046 and 1998 cm^{-1} in complex **5** confirm the presence of two different types of azide ligands in this compound (terminal and bridging, respectively).[4,7] It is noteworthy that the absence of an azide peak in the FT-IR spectra of complexes **2** and **3** indicates the absence of azide groups in the structure of these complexes. In complex **4**, the two new characteristic bands at 2068 cm^{-1} and 2115 cm^{-1} are assigned to the $\nu_{as}(C\equiv N)$ stretching of SCN^- groups. Generally, S-bonded complexes display the $\nu_{as}(C\equiv N)$ above 2100 cm^{-1}, while N-bonded complexes show the band below that.[5,14] The FT-IR spectrum of complex **4**, with peaks at 2068 and 2115 cm^{-1}, suggests that the anionic thiocyanate co-ligands are coordinated *via* both nitrogen and sulfur atoms. These assignments were further confirmed by the X-ray structural analyses (Section 3.3).

As previously documented in the literature,[25–27] ^{31}P NMR spectroscopy is an effective method for determining the coordination mode of phosphorus ylides. The ^{31}P NMR chemical shifts for all studied complexes (**1–5**) occur at higher frequencies than the free ylide (**L**), suggesting coordination through the ylidic carbon. Notably, complexes **1** and **5** each exhibit a singlet peak around 17.93 (Fig. 2a) and 20.26 ppm, respectively, while complex **4** displays two singlet peaks at 21.92 and 23.75 ppm, indicating the presence of two distinct structures (Fig. 2b).

In the ^{1}H NMR spectra, the signal related to the methinic proton (PCH) of phosphorus ylide complexes is the most reliable method for determining the coordination mode of a

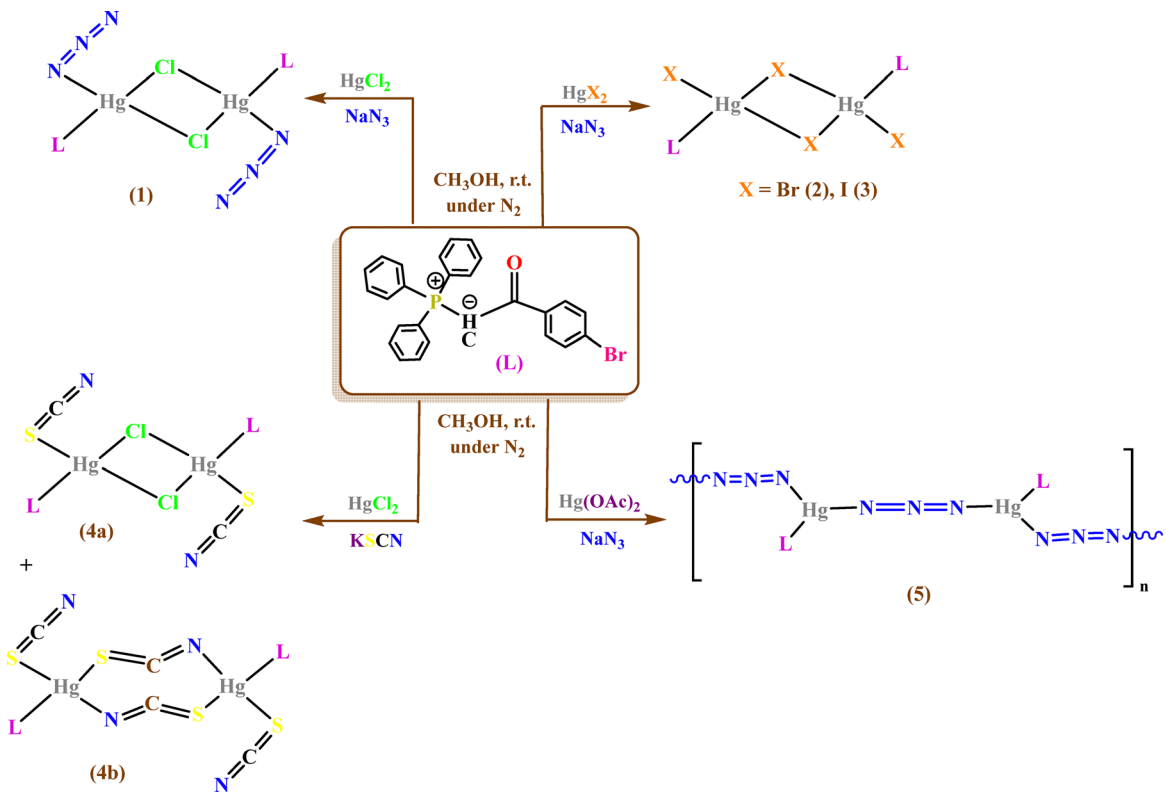

Scheme 1 Schematic of the synthetic routes for all the complexes studied herein.

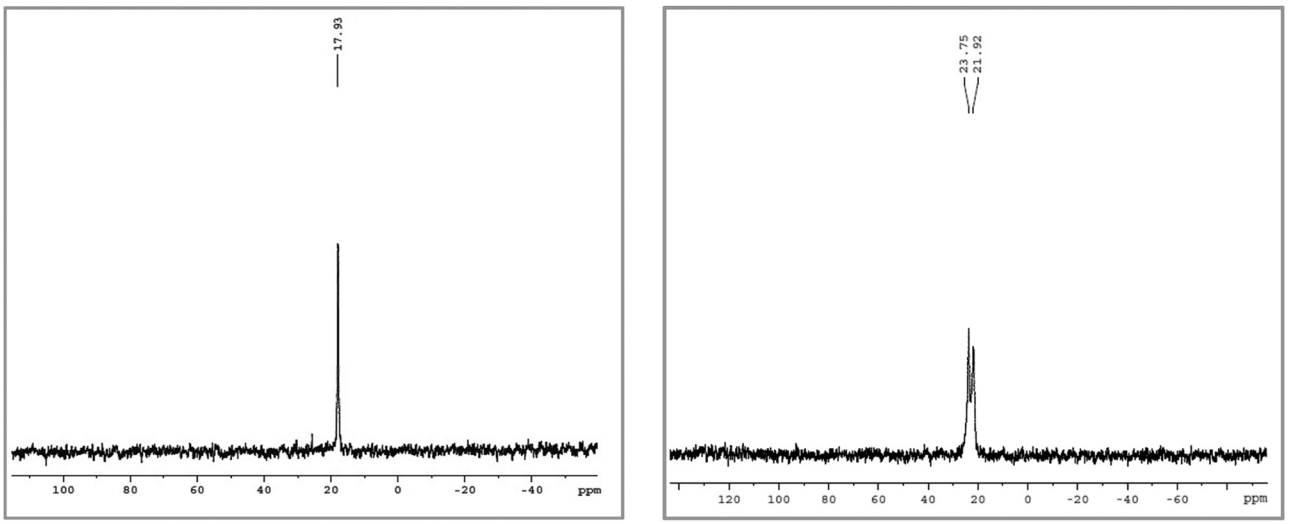

Fig. 2 $^{31}P\{^{1}H\}$ NMR spectra of (a) complex **1** and (b) complex **4**.

ylide to a metal center.[21] The ^{1}H NMR spectra of complexes **1**, **4** and **5** (≈5 ppm) display a downfield shift of the CH signals with respect to the parent ylide,[25–27] which is attributed to the C-coordination mode of the phosphorus ylide. Furthermore, the characteristic peaks of carbonyl and methinic groups in the ^{13}C NMR spectra of complexes **1**, **4** and **5** show downfield shifts with respect to the parent ylide (**L**).[20] Accordingly, the spectral data clearly show that the ligand, *via* the ylidic carbon atom, is coordinated to mercury(II) ions, and these complexes also contain azide and thiocyanate co-ligands.

3.3. Description of the structures

3.3.1. Crystal structure of the phosphorus ylide ligand (L). Crystals of the phosphorus ylide ligand (**L**), namely, 4-bromobenzoylmethylenetriphenylphosphorane ylide, [$Ph_3PC(H)$-$C(O)C_6H_4$-*p*-Br], were obtained by vapor diffusion of diethyl ether into chloroform. The resulting crystals were found to be identical in structure to those previously obtained from acetonitrile–diethyl ether (Fig. S19).[59] The structure shows that the P–C(1) and C(1)–C(2, sp^2) bond lengths are shorter than the typical P^+–C(sp^3) and C–C values (1.800 and 1.511 Å, respectively),[60] while the C=O bond distance is longer than the usual value (1.210 Å),[60] indicative of ylidic resonance in the ligand (see Table S1). The geometry around the P atom is nearly tetrahedral, with the O atom oriented *cis* to the P atom.

3.3.2. Crystal structure of complex 1. The dimeric mercury–azide complex, namely, bis [(4-bromobenzoylmethyl) triphenylphosphonium]di-μ-chlorido-bis[diazidomercurate], [$LHg(N_3)\mu$-$Cl]_2$ (**1**), was obtained by the reaction between the phosphorus ylide ligand (**L**), $HgCl_2$ and NaN_3 in a methanol solution. A perspective view of **1**, together with the partial atom numbering scheme, is depicted in Fig. 3.

Complex **1** crystallizes in the monoclinic $P2_1/c$ space group with $Z = 2$ (Table 1). This complex has a dinuclear structure with the mercury atom in a distorted tetrahedral environment

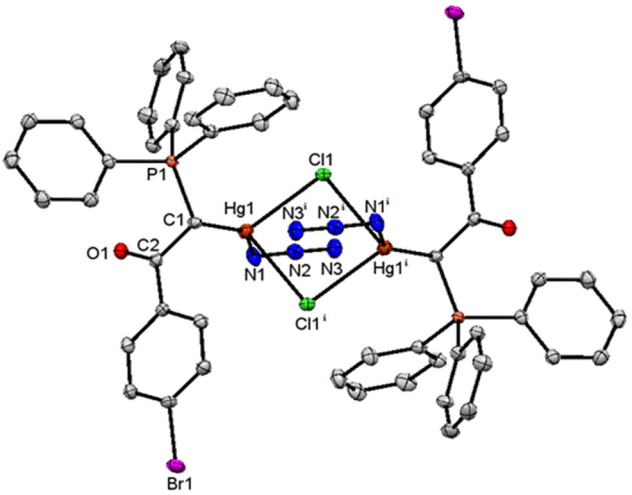

Fig. 3 Molecular diagram of complex **1** together with atom labelling. Hydrogen atoms are omitted for clarity. Symm code (i): $1-x, 1-y, 1-z$.

coordinated by the ylide carbon atom of the ligand, two chloride atoms (each of which is bridging to another Hg atom), and a terminal azide anion. The molecule lies across a centre of symmetry, so the Hg_2Cl_2 unit is planar, with the Hg–Cl–Hg and Cl–Hg–Cl angles being close to 90° (Table 2). The two Hg–Cl distances are different, while the Hg–C and Hg–N distances are similar. The Hg(1)···Hg(1) distance of 3.846 Å is greater than the sum of the covalent radii of two mercury atoms (2.98 Å)[61] and is comparable to distances observed in other dimeric halogen-bridged complexes.[26,27] This observation reveals that the interaction between the two mercury atoms is predominantly noncovalent in nature. The distortion from the regular tetrahedral geometry can be seen from the angles around the Hg atom, ranging from 88.62(3)° to 145.35(14)°. Continuous shape measure (CShM) calculations show that the geometry is

Table 3 Shape indices[62,63] for the coordination environment around the mercury atom in the studied complexes

Complex	T_d	C_{2v}	C_{3v}
1	2.620	5.018	2.783
3	1.346	8.216	1.945
4a	1.856	5.470	1.527
4b	2.110	6.111	1.394
5	4.261	2.279	4.479

T_d: tetrahedron; C_{2v}: seesaw; C_{3v}: vacant trigonal bipyramid.

intermediate between a tetrahedron and a vacant trigonal bipyramid (Table 3).[62,63] The Hg atom lies 0.193(2) Å above the plane of the three coordinating atoms C1, Cl1 and N1. The azide groups are oriented such that they lie above and below the Hg_2Cl_2 unit, directed towards a point midway between the Cl atom and the Hg atom located across the centre of symmetry. The structure of compound **1** exhibits two distinct types of hydrogen bonds: intramolecular and intermolecular (Table 4 and Fig. S20). The intramolecular nonclassic C–H···N, C–H···Cl, and C–H···O hydrogen bonds contribute to the stabilization of the dimeric moiety. In contrast, the intermolecular hydrogen bonds C–H···N (2.34 Å) and C–H···O (2.58 Å) connect the dimeric units in three dimensions, forming a three-dimensional hydrogen bond network (Fig. S21). The structure is similar to the mercury complex with the 4-nitrophenyl–substituted ylide ligand we previously isolated, bis(μ-chloro)-diazido-bis[2-(4-nitrophenyl)-2-oxo-1-(triphenylphosphonio)ethyl]-di-mercury.[43] The major difference is that the azide anion is oriented away from the Hg_2Cl_2 unit, with the Cl1–Hg1–N2–N3 torsion angle being 154.1(8)°, compared to the torsion angle of 22.5(2)° found here for complex **1**.

A search through the Cambridge Structural Database[28] found only two other structures with an Hg_2Cl_2 unit where the mercury is also coordinating to a carbon atom and a nitrogen atom, and neither of them are azides. However, there are 43 mercury–azide structures, six of which are simple alkyl mercury azide compounds. Only one is a halogen-bridged complex, the [(μ$_2$-azido-*N*1,*N*1)-(μ$_2$-chloro)-azido-mercury]$^{2-}$ anion,[28] where the angles range around the Hg range from 89.799(19)° to 150.4(2)°, similar to those found here, but with the azides oriented away from the Hg_2Cl_2 moiety.

A comparison of the geometrical parameters of complex **1** with the parent ylide (**L**) reveals that the P1–C1 bond length in the complex is longer than that of the ylide, while the C2–O1 distance is shorter. This indicates that the resonance stability of **L** is disrupted upon complex formation, leading to a loss of electron delocalization in the P1–C1–C2═O1 structure due to the coordination of ylidic carbon (C1) with the mercury center.

3.3.3. Crystal structure of complex 3. The mercury–iodio complex bis [(4-bromobenzoylmethyl) triphenylphosphonium]di-μ-iodido-bis[diiodidomercurate], $[LHgI(\mu\text{-}I)]_2$, crystallizes in the triclinic system with the space group $P\bar{1}$ and $Z = 1$ (Table 1). Fig. 4 illustrates the molecular structure, and Table 2 lists the selected bond lengths and bond angles around the central metal ions, which are close to those of previously reported similar structures.[64]

This complex is a dinuclear structure with the mercury atom in a distorted tetrahedral environment coordinated by the ylidic carbon atom of the ligand, two iodide atoms (each of which is bridging to another Hg atom), and a terminal iodide. The molecule lies across a centre of symmetry, so the Hg_2I_2 unit is planar, with the Hg–I–Hg and I–Hg–I angles being close to 90°. The two bridging Hg–I distances are different but longer

Table 4 Hydrogen bonds in complexes **1**, **3**, **4a**, **4b** and **5**

D–H···A	D–H/Å	H···A/Å	D–A/Å	D–H···A/°
(**1**)				
C1–H1···N3^a	1.00	2.56	3.431(5)	145
C18–H18···N3^b	0.95	2.58	3.434(6)	150
C20–H20···Cl1	0.95	2.68	3.605(5)	164
C22–H22···O1	0.95	2.55	3.347(5)	142
C25–H25···O1^c	0.95	2.34	3.210(5	152
(**3**)				
C20–H20···O1	0.95	2.30	3.111(4)	144
C24–H24···O1^d	0.95	2.55	3.220(5)	128
(**4a**)				
C1–H1···N1^a	1.00	2.50	3.395(5)	149
C11–H11···N1^b	0.95	2.61	3.241(5)	124
C20–H20···Cl1	0.95	2.77	3.669(4)	158
C22–H22···O1	0.95	2.46	3.274(4)	144
C25–H25···O1^e	0.95	2.44	3.354(4)	161
(**4b**)				
C19–H19···O1^f	0.95	2.54	3.271(4)	134
C22–H22···O1	0.95	2.59	3.313(3)	133
C22–H22···N2^a	0.95	2.43	3.244(4)	144
C24–H24···S2^g	0.95	2.85	3.723(3)	154
(**5**)				
C1–H1···N4^h	1.00	2.44	3.438(6)	173
C8–H8···N5	0.95	2.62	3.147(5)	116
C8–H8···N4^h	0.95	2.60	3.399(6)	142
C17–H17···N2^i	0.95	2.46	3.267(7)	143
C17–H17···N3^i	0.95	2.61	3.401(8)	141
C22–H22···O1	0.95	2.53	3.142(6)	122

^{a} $1-x, 1-y, 1-z$. ^{b} $x, 3/2-y, 1/2+z$. ^{c} $-1+x, y, z$. ^{d} $1+x, y, z$. ^{e} $-1+x, y, -1+z$. ^{f} $x, 1+y, z$. ^{g} $\frac{1}{2}+x, 3/2-y, 1-z$. ^{h} $1/2-y, 1/2-x, 1/2+z$. ^{i} $x, y, 1+z$.

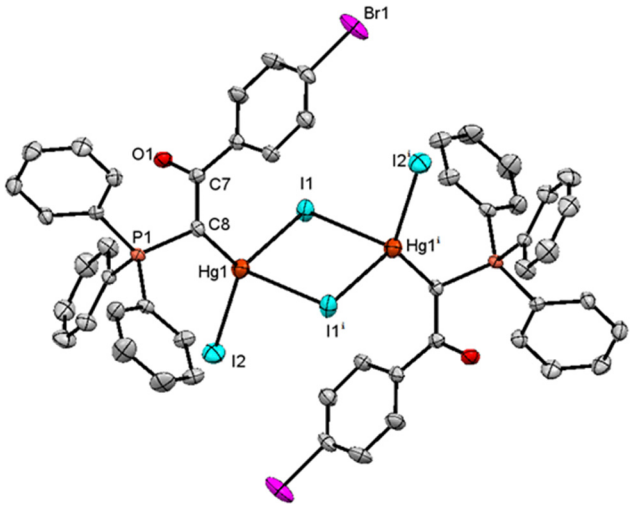

Fig. 4 Molecular diagram of **3** together with the atom numbering scheme. Hydrogen atoms are omitted for clarity. Symm code (i): $1-x, 1-y, 1-z$.

than the terminal Hg–I distance (Table 2). The distortion from the regular tetrahedral geometry can be seen from the angles around the Hg atom, ranging from 92.19(3)° to 125.46(8)°, CShM calculations show that the geometry is closer to a tetrahedron than a vacant trigonal bipyramid (Table 3).[62,63] The Hg atom lies 0.2807(12) Å above the plane of the three coordinating atoms C1, I1 and I2. The structure of compound **3** also reveals both intramolecular and intermolecular C–H···O interactions (Table 4 and Fig. S22). The intermolecular C–H···O hydrogen bonds (2.55 Å) connect the dimeric units side by side, resulting in the formation of hydrogen-bonded one-dimensional polymeric chains running along the *a*-axis (Fig. S23). The structure of **3** is similar to that reported for bis(μ_2-iodido)-bis[(4-fluorobenzoyl)(triphenylphosphonio)methanide]-di-iodido-di-mercury(II).[65] The Hg–C bond length in complex **1** (2.175(5) Å) is shorter than that found in complex **3** (2.287(3) Å), indicating relatively strong bonds in dimeric mercury–azide complexes compared to halide-bridged complexes. This shortening of the Hg–C bond can be attributed to the use of mercury orbitals with high *s* characters for bonding to the ylidic carbon. Additionally, the involvement of these high-s-character orbitals allows for a more effective delocalization of the electron density, which further contributes to the overall stability of the complex.

3.3.4. Crystal structure of complexes 4a and 4b. The treatment of mercury chloride with one equivalent of **L** in excess KSCN produces dimeric mercury–thiocyanide complexes (**4a** and **4b**).[5,8] Fig. 5 displays an ORTEP view of these complexes, along with their atom numbering schemes. Selected bond distances and angles are listed in Table 2. Upon evaporation of the solution, two different crystals are found, [LHg(SCN)μ-Cl]$_2$ (**4a**) and [LHg(SCN)μ-SCN]$_2$ (**4b**).

*Complex **4a**.* The complex crystallizes in the monoclinic space group $P2_1/c$ with Z = 2. The Hg(II) atom is bonded to one carbon atom from the methine ylide (Hg–C distance: 2.198(3) Å), one sulfur atom from the terminal thiocyanate ligand (Hg–S distance: 2.4683(9) Å), and two bridged chloride ions. As anticipated, the Hg–C bond length is significantly shorter than the Hg–S and Hg–Cl bond lengths. The crystal

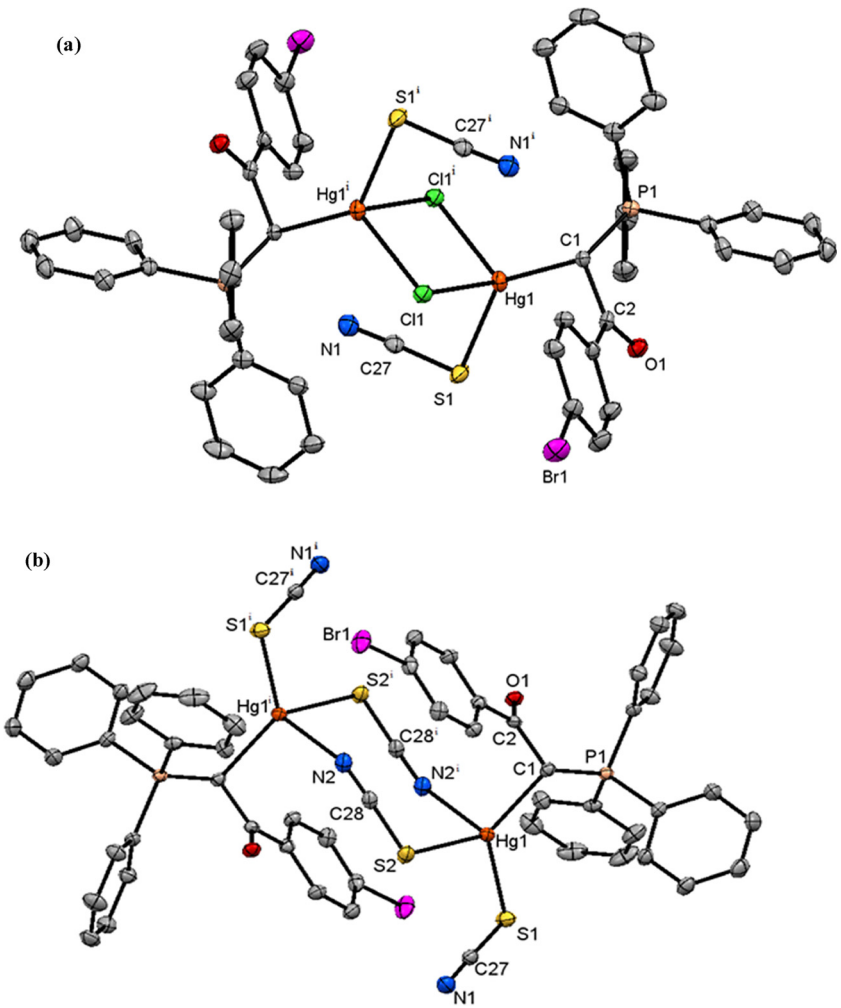

Fig. 5 Molecular diagrams of complexes (a) **4a** and (b) **4b** together with atom labelling. Hydrogen atoms are omitted for clarity. Symm code (i): 1 − *x*, 1 − *y*, 1 − *z*.

structure of **4a** is isomorphous with complex **1**, with only slight changes in cell dimensions to account for the larger thiocyanate anion (Fig. 5a). The main difference in the structure is a longer Hg–S distance (Hg1–S1: 2.4683(9) Å), due to the coordination of a sulfur atom in place of a nitrogen atom, and a much smaller C1–Hg1–S1 angle. This leads to less distortion from the ideal tetrahedral geometry, with angles around the Hg atom in the range of 89.46(2)°–134.71(8)°. However, CShM calculations show that the geometry lies closer to a vacant trigonal bipyramid rather than to a tetrahedron (Table 3);[62,63] the Hg atom lies 0.1923(13) Å above the plane of the three coordinating atoms C1, S1 and N1. Further, the thiocyanate anion is oriented closer to the chloride atom than to the Hg atom situated across the centre of symmetry. The structure of compound **4a** also shows both intramolecular C–H···X (X = O, N and Cl) and intermolecular C–H···O interactions (Table 4 and Fig. S24). In contrast to the structure of **1**, the intermolecular C–H···O (2.44 Å) interactions in **4a** link the dimeric units in the crystallographic *bc* plane, forming two-dimensional polymeric sheets (Fig. S25 and S26). There is only one known mercury thiocyanate structure with an Hg_2Cl_2 unit, $[(SCN)_2HgCl]_2$,[66] while there were only two organomercury structures,[67,68] both of which have the sulfur atom of the thiocyanate bridging two mercury atoms.

*Complex **4b**.* The complex crystallizes in the orthorhombic space group *Pbca* with $Z = 4$ (Table 1). In complex **4b**, the Hg–S(2) and Hg–N(2) bond lengths for the thiocyanate-bridging ligand are almost identical) 2.5303(7) Å and 2.533(2) Å, respectively(. The Hg–S distances related to terminal and bringing thiocyanate ligands are unequal and lie in the range of 2.5014–2.5303 Å (Table 2). The Hg–S distances lie in the range of the reported values.[69] This complex features a dinuclear structure, where each Hg atom is coordinated by one ylidic carbon, one sulfur atom from a terminal thiocyanate anion, and one sulfur atom and one nitrogen atom from two thiocyanate anions that are bridging to another Hg atom across the centre of symmetry (Fig. 5b). The bridging thiocyanate anions and Hg atoms form an 8-membered ring, which adopts a chair conformation with the Hg atoms lying 1.137(3) Å above and below the plane of the six thiocyanate atoms. The terminal thiocyanate anion is oriented away from the 8-membered ring, close to the sulfur atom of the bridging thiocyanate (S2–Hg1–S1–C27: −17.05(10)°). CShM calculations show that the geometry around the Hg atom lies between a tetrahedron and a vacant trigonal bipyramid, but closer to a vacant trigonal bipyramid (Table 3).[62,63] The Hg atom lies 0.2781(11) Å out of the plane of the three coordinating atoms C1, S1 and S2. The hydrogen bond interactions in complex **4b** are almost similar to those in structure **3** (Table 4 and Fig. S27). The intramolecular C–H···O and C–H···N interactions stabilize the dimeric units, while intermolecular C–H···O interactions (2.54 Å) connect the dimeric units in the crystallographic *b* direction, leading to the formation of hydrogen-bonded one-dimensional polymeric chains (Fig. S28).

Complex **4b** is similar to bis((μ$_2$-thiocyanato)-(1,3-benzothiazol-2-amine)-thiocyanato–mercury(II)),[30] where the thiocyanate ligand lies above the $[Hg(SCN)]_2$ group, and the corresponding torsion angle S2–Hg1–S3–C9 is −42.09(17)°. There is only one structure with an Hg_2Cl_2 unit, $[(SCN)_2HgCl]_2$,[66] while there are only two organomercury structures,[67,68] both of which have the sulfur atom of the thiocyanate bridging two mercury atoms.

3.3.5. Crystal structure of complex 5. This compound has a polymeric structure and crystallizes in the tetragonal system in the space group $P42_1c$ and $Z = 8$ (Table 1). The monomeric unit of the 1D chain of complex **5** is illustrated in Fig. 6, and the bond parameters are listed in Table 2. In this structure, the Hg atom is coordinated by the ylidic carbon from the ligand, one nitrogen from a monodentate azide and two nitrogen atoms from azides that are bridging to other Hg atoms (Fig. 6), resulting in a 1D azide-bridged polymer along the *c*-axis (Fig. 7). In this structure, azide ions act as both bridging bidentate and terminal monodentate ligands. In the bridging azide groups, the Hg–N(4) and Hg–N(6) bond distances are relatively different) 2.488(4) Å and 2.606(4) Å, respectively(. The Hg–N distance involving the terminal azide is much shorter than the Hg–N distance involving the bridging azide ligands (Table 2), and these two distances show that the azide is coordinating asymmetrically to the Hg atoms. It is noteworthy that the bridging bidentate ligand azide binds the mercury *via* the end-to-end (EE) coordination mode. The angles around the Hg atom vary substantially from 89.67(14)° to 161.47(16)°. CShM calculations[62,63] indicate that the coordination environment surrounding the Hg atom is closer to a seesaw geometry (Table 3) than a tetrahedral geometry. The Hg atom lies 0.148(3) Å above the plane of the three coordinating atoms C1, N1 and N4. The structure of **5** only shows intramolecular nonclassic C–H···N and C–H···O hydrogen bonds (Table 4),

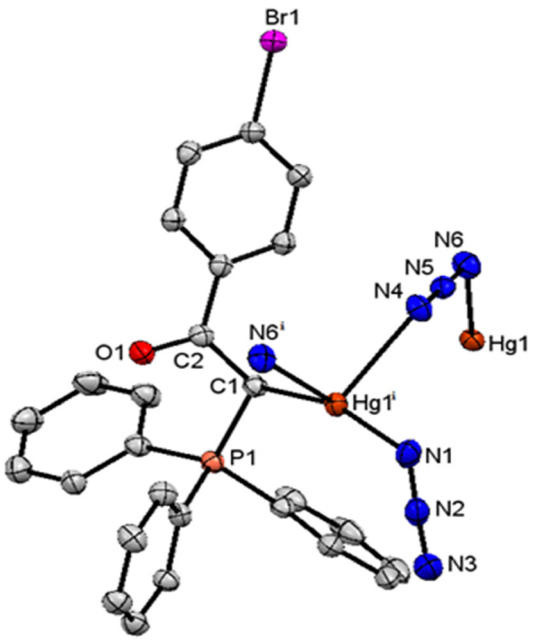

Fig. 6 ORTEP diagram of the coordination environment around the Hg atom in $[LHg(N_3)\mu\text{-}N_3]_2$ (**5**). Hydrogen atoms are omitted for clarity. Symm code: (i): 1/2 − *y*, 1/2 − *x*, −1/2 + *z*.

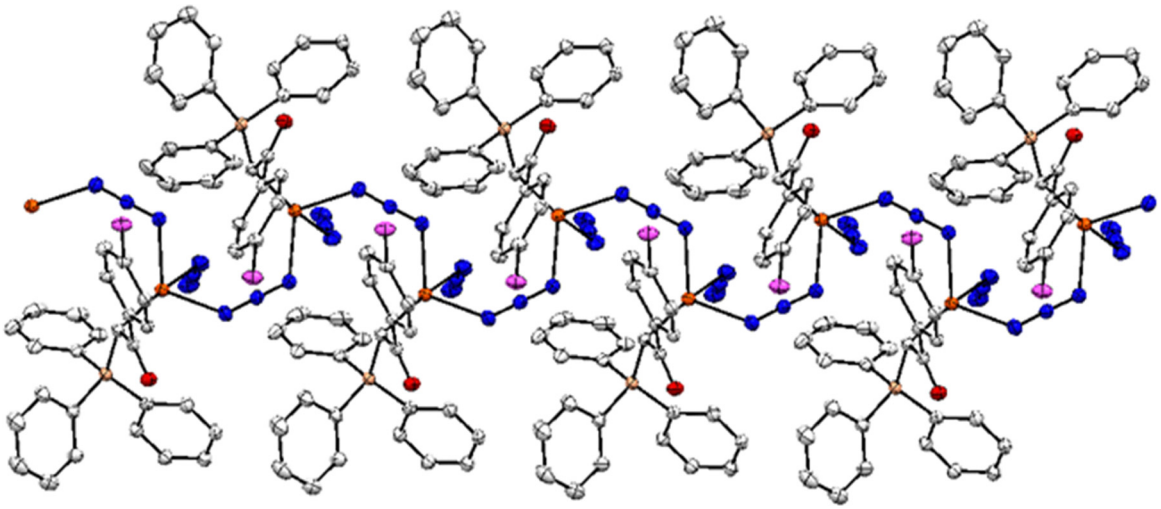

Fig. 7 ORTEP diagram showing a portion of the 1D Hg–N_3–Hg chain of complex **5**. Hydrogen atoms are omitted for clarity. Only the Hg and N atoms are labelled. Symm code: (i): 1/2 − *y*, 1/2 − *x*, −1/2 + *z*; (ii): 1/2 − *y*, 1/2 − *x*, 1/2 + *z*.

which contribute to the stabilization of the polymeric chains (Fig. S29). In contrast to compounds **1–4**, the hydrogen bond interactions in the structure of **5** do not induce any changes in the structural dimensions of this compound. The only mercury complexes with bridging azides are $[Hg(N_3)_2(\mu_2\text{-}N_3)]_n^-$ (ref. 70) and *catena*-[bis(μ$_3$-azido-*N*1,*N*1,*N*3)-bis(μ$_2$-azido-*N*1,*N*1)-bis(*N*-(2-methoxyphenyl)-1-(pyridin-2-yl)methanimine)-diazido-trimercury(II)];[71] the only organomercury complexes with monodentate azides are six simple alkyl mercury azide compounds.

3.4. Antibacterial activity of the complexes (1–5)

The antibacterial potential of complexes **1–5** is presented in Table 5. All tested compounds showed high antibacterial activity and were able to inhibit bacterial growth. Among these compounds, complexes **4** and **5** showed the lowest MIC and MBC values, indicating their greater antibacterial potential compared with other complexes. However, complex **1** also had high antibacterial activity, which was followed by complexes **2** and **3**. The inhibitory effect of complex **1** on Gram-positive species was much higher than that on Gram-negative ones. *B. subtilis* was the most sensitive species to this compound, as the MIC of this complex against it was less than 6.25 μg mL^{-1}. Interestingly, the MBC value of complex **1** against this species was the lowest (50 μg mL^{-1}) compared with other tested bacteria. However, other bacterial species were sensitive to this complex, and low MIC and MBC values were found for these bacteria also. Complex **1** has azide in its structure, and the high antibacterial activity of this compound is related to its presence. Azide is an electron transport inhibitor that can interfere with electron carriers in the cytoplasmic membrane of bacteria and hence inhibits the electron transport phosphorylation (ETP) process in bacteria. ETP is the main mechanism for energy (ATP) production during bacterial metabolism that depends on different electron carriers, and any disturbance of the sequential electron transport can cause loss of energy in bacterial cells. Consequently, the energy charge (EC) of bacterial cells will be reduced below what is needed for multiplication, growth and division, which finally leads to bacterial death.[72] The higher sensitivity toward Gram-positive bacteria than Gram-negative species may be due to the difference in their cell structure. In Gram-negative bacteria, the presence of an outer membrane (OM) can limit complex access to its target,

Table 5 MIC and MBC indices of mercury complexes as determined by the macrobroth dilution method

	Gram-negative				Gram-positive			
	Escherichia coli		*Pseudomonas aeruginosa*		*Bacillus subtilis*		*Staphylococcus aureus*	
Compound	MIC	MBC	MIC	MBC	MIC	MBC	MIC	MBC
L	200<	—	200<	—	200<	—	200<	—
1	100 μg	200 μg	12.5 μg	200 μg	<6.25 μg	50 μg	12.5 μg	200 μg
2	<200 μg	—	25 μg	200 μg	<12.5 μg	25 μg	50 μg	<200 μg
3	100 μg	100 μg	50 μg	50 μg	25 μg	25 μg	100 μg	100 μg
4	6.25 μg	12.5 μg	6.25 μg	12.5 μg	12.5 μg	25 μg	12.5 μg	25 μg
5	6.25 μg	6.25 μg	6.25 μg	12.5 μg	12.5 μg	25 μg	6.25 μg	12.5 μg
$HgCl_2$	6.25 μg	6.25 μg	6.25 μg	25 μg	6.25 μg	6.25 μg	6.25 μg	25 μg
$HgBr_2$	6.25 μg	6.25 μg	6.25 μg	25 μg	6.25 μg	6.25 μg	6.25 μg	25 μg
HgI_2	6.25 μg	6.25 μg	6.25 μg	25 μg	6.25 μg	6.25 μg	6.25 μg	25 μg
$Hg(OAc)_2$	6.25 μg	25 μg	6.25 μg	50 μg	6.25 μg	25 μg	6.25 μg	50 μg

while in Gram-positive bacteria, the cell wall is directly in contact with the surrounding environment, and hence, the test compound can more easily access the target site. The presence of Hg in this and other tested compounds also affords antibacterial properties to these complexes. Hg can bind to the sulfhydryl group in bacterial enzymes and inhibit the functions related to them, *i.e.*, metabolism, energy production and multiplication. While the antibacterial effects of complexes **2** and **3** were less than those of complex **1**, they showed high antibacterial activity and were able to inhibit and/or kill target bacteria at low concentrations. This difference is primarily due to the lack of azide in the structure of complexes **2** and **3**. In the case of complex **3**, the MIC was equal to the MBC for each bacterial species. This reveals that this complex at the mentioned concentrations has bactericidal activity and kills target bacteria, while the cases with two different values for MIC and MBC reveal that the complex can inhibit bacterial growth at the MIC concentration and kill bacterial cells at the MBC concentration. In other words, complex **1** can act as a bacteriostatic or bactericidal agent at different concentrations, while complex **3** acts as a bactericidal agent. The observed differences between complexes **2** and **3** may be due to the type of halogen (Br and I, respectively) in their structure. They are oxidizing agents that can damage macromolecular structures in target bacteria and inactivate them. So, halogenation can increase the antibacterial properties of the synthesized complexes.[73] In case of complexes **4** and **5**, the highest antibacterial activity was found against the tested bacterial species. The higher antibacterial activity of complex **4** is due to the presence of cyanide in this complex. Cyanide is an inhibitor of cytochromes, which are involved in the final step of the electron transport chain and electron delivery to the final electron acceptor, *i.e.*, molecular oxygen. Diverse cytochromes are involved in this process, and there is significant diversity among bacterial species with regard to these cytochromes. During this electron transport to the final electron acceptor, H^+ ions are excreted out of the bacterial cell which creates a proton gradient outside the bacterial cell. This gradient forms the proton motive force (PMF), and as a result of protons moving back to the cytoplasm, the energy in the form of ATP will be generated. Furthermore, this gradient provides the required energy for bacterial movement and absorption and secretion of nutrients and products. As a result of the inhibition of cytochromes, the PMF will be impaired, and all metabolic reactions, which are dependent on PMF, will be stopped. Hence, complex **4** showed more antibacterial activity than the other compounds. However, the presence of cytochrome *d* in some bacterial species is responsible for their tolerance to cyanide, and bacterial growth may therefore not be affected. This cytochrome has low affinity for binding with cyanide, and hence, the bacteria that have this type of cytochrome are tolerant to cyanide.[72] The polymeric structure of complex **5**, due to its large molecular structure as well as the presence of several moieties of azide in the complex, shows high antibacterial potential. The large molecular structure of this complex can disrupt the molecular structure of the bacterial envelope (*i.e.*, cytoplasmic membrane, cell wall and outer membrane), and regarding the vital role of these structures in bacterial growth and division, growth inhibition and bacterial cell death will result.[72]

The size, 3D structure and degree of lipophilicity of complexes can directly affect their access to the target site and affect their antibacterial activity. The bacterial cell is enveloped with the phospholipid bilayer cytoplasmic membrane and peptidoglycan cell wall. In Gram-negative bacteria, furthermore, an outer membrane surrounds all these structures. The thickness and chemical structures of these envelopes vary among different bacterial species, but they provide, overall, a semipermeable barrier that selectively controls the uptake and secretion of nutrients and chemicals by bacterial cells. Transfer through the outer membrane and cytoplasmic membrane is directly correlated with the size and lipophilicity of the compound because the phospholipid bilayer in the cytoplasmic membrane and the phospholipid and lipopolysaccharide bilayer structures in the outer membrane create a hydrophobic structure that limits diffusion through them. So, more lipophilicity can promote diffusion through the outer membrane and cytoplasmic membrane. The molecular size of the compound also affects this diffusion because lipid packaging in these membranes tries to maintain the membrane fluidity and integrity. So, the insertion of large molecular structures within these membranes can disrupt this packaging and membrane integrity. In the case of the cell wall, several peptidoglycan layers are present on the outside of the cytoplasmic membrane, which varies from 1–3 layers in Gram-negative bacteria to 40 layers in Gram-positive bacteria. The peptide cross-links between these layers create a net-like structure with pores within it, which facilitates the diffusion of substances toward the cell membrane and cytoplasm. The notifiable subject is that these pores do not align with the others, and hence, a corkscrew duct will be created. So, in addition to the molecular size of the compound, its 3D structure is of great importance in order to be transported across the cell wall and get access to its target(s).[74–77] The tested bacterial species showed different sensitivities to these compounds, and this was reflected in the differences in their MIC and MBC indices. The results can be found in Table 5 and Fig. 8. It should be noted that compound 301 in the laboratory images is the same as complex **1** in this research. The effect of some reference antibiotics was also investigated against target bacteria using the disc diffusion assay method. As can be found from Table 6, *B. subtilis* was resistant to ceftriaxone, ceftizoxime and cephalexin, *S. aureus* was resistant to enrofloxacin, and *E. coli* and *P. aeruginosa* were resistant to cephalexin. All bacterial species were resistant to cloxacillin. A comparison of the results of standard antibiotics with synthesized compounds shows that in spite of antibiotic resistance against some antibiotics in different species, all compounds in the present study were able to inhibit bacterial growth and/or kill them even at very low concentrations, which have been expressed as the MIC and MBC, respectively. So, these compounds can be good candidates for the eradication of antibiotic-resistant strains that may be found in environments, especially in common settings such as hospitals or diagnostic laboratories.

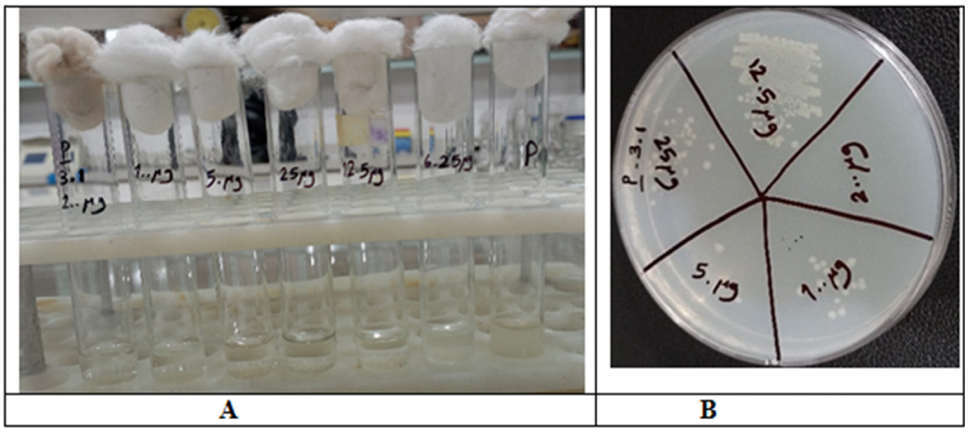

Fig. 8 (A) Macrobroth dilution method for determining the MIC index for complexes; lack of turbidity indicates bacterial growth inhibition. (B) MBC determination; lack of colony formation from growth negative tubes indicates the bactericidal activity of the complex.

Table 6 Antibacterial susceptibility assay of bacteria against standard antibiotics

	Gram-negative		Gram-positive	
Compound	*E. coli*	*P. aeruginosa*	*B. subtilis*	*S. aureus*
Gentamicin	18[a]	17	19	25
Ceftriaxone	25	24	—	21
Ceftizoxime	23	23	—	9
Tetracycline	21	23	20	30
Cephalexin	—	—	—	10
Enrofloxacin	30	30	27	—
Imipenem	18	40	28	25
Cloxacillin	—	—	—	—

[a] Inhibition zone diameter (mm).

3.5. Antifungal activity bioassay

The results of the antifungal assay showed that all complexes were able to inhibit fungal growth at both tested concentrations. At a 500 μg mL^{-1} concentration, the fungal species were not completely inhibited, their growth was only retarded, and less turbidity was achieved following incubation compared with the positive control (Fig. 9a). However, at a 1 mg mL^{-1} concentration, both fungal species were completely inhibited, no fungal growth was evidenced in the broth, and no colony was formed on agar (Fig. 9b). So, the MICs and minimum fungicidal concentrations (MFCs) for all complexes against the tested fungal species were equal to 1 mg mL^{-1} (Table 7). Thus, all of the synthesized complexes are fungicidal agents that can be used for fungal growth inhibition in the environment. It should be noted that compound 304 in the laboratory images is the same as complex **2** in this research.

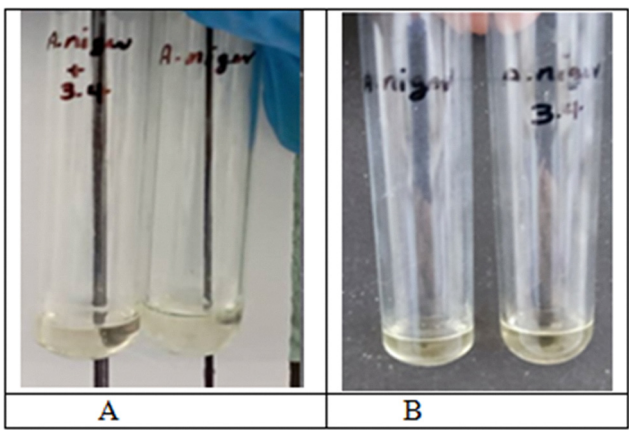

Fig. 9 Antifungal activity of complex **3** against *Aspergillus niger* at 500 μg mL^{-1} (A) and 1 mg mL^{-1} (B) concentrations. Lack of turbidity in test tubes compared with controls indicates growth inhibition.

Table 7 MICs and MFCs (mg mL^{-1}) of complexes against the studied fungi

	Fungi	
Compound	*Aspergillus niger*	*Aspergillus flavus*
1	MIC = MFC = 1	MIC = MFC = 1
2	MIC = MFC = 1	MIC = MFC = 1
3	MIC = MFC = 1	MIC = MFC = 1
4	MIC = MFC = 1	MIC = MFC = 1
5	MIC = MFC = 1	MIC = MFC = 1

In the antibiotic susceptibility assessment of the target fungi to standard antifungal agents, it was found that both *A. niger* and *A. flavus* were resistant to fluconazole, and *A. niger* was resistant to amphotericin B (Table 8). Further, all synthesized compounds completely inhibited and killed these fungi at a 1 mg mL^{-1} concentration, *i.e.*, their MIC was equal to the MFC. These results confirm that the synthesized compounds can overcome antifungal resistance and hence can be a suitable choice for developing new antifungal agents that can be used

Table 8 Antifungal effect of standard antibiotics against target fungi

	Fungi	
Compound	*Aspergillus niger*	*Aspergillus flavus*
Fluconazole	—	—
Miconazole	19[a]	20
Itraconazole	14	15
Amphotericin B	—	14
Nystatin	26	27

[a] Inhibition zone diameter (mm).

for fungal growth control in the environment as well as in industrial processes. This potential suggests that fungal growth inhibition may be due to metabolic interference by the synthesized compounds, and if such a mechanism is involved, these compounds will be good candidates for the inhibition of mycotoxin production by mycotoxigenic fungi.

Conclusion

In this work, we have successfully designed, synthesized and characterized five dinuclear and polymeric mercury complexes through the one-pot reaction of $[Ph_3PC(H)C(O)C_6H_4$-*p*-Br] (**L**) with mercury(II) salts (HgX_2 and $Hg(OAc)_2$) in methanol using excess amounts of two different pseudo-halides, N_3^- and SCN^-. There is a good agreement between the spectroscopic properties and structures of the compounds. From X-ray diffraction and spectroscopic analyses, it is concluded that the final structures depend on the type of mercury salt and anionic co-ligand. Under the same conditions, with sodium azide, mercury(II) chloride yields a dimeric mercury–azide complex (**1**), mercury(II) bromide and iodide form dimeric halide-bridged complexes (**2** and **3**), and mercury acetate affords an azido-bridged polymeric complex (**5**). Also, azide anions act as terminal ligands (**1**), while thiocyanate serves as both a bridging and terminal co-ligand under similar reaction conditions (**4a** and **4b**). Non-classical hydrogen bonds play intriguing roles in crystal packing and the dimensionality of structures, leading to the formation of one- to three-dimensional hydrogen-bonded polymeric architectures. The dominant structural feature of **1**, **2**, and **3** is the $[LHg(\mu\text{-}X)]_2$ core, with the azide able to replace only the terminal chloride in **3**. In **4**, although thiocyanate is expected to bind preferentially to Hg, the $[LHg(\mu\text{-}Cl)]_2$ core persists; the reaction products are partly a mixture of chloride-bridged (**4a**) and thiocyanate-bridged (**4b**) complexes. An azide-only complex is formed only when acetate is the counter-anion, indicating that the choice of mercury salt strongly influences the final product. In particular, the $[LHg(\mu\text{-}Cl)]_2$ core appears to be highly stable even in the presence of thiocyanate, which mercury would normally prefer. The only reliable way to obtain halide-free products is to start from mercury salts that contain no halides. The biological performance of the synthesized compounds was examined against two species of Gram-positive and Gram-negative bacteria as well as two fungi. This research highlights the profound impact of phosphorous ylide ligand variability, the choice of starting materials and interaction modalities in the design of mercury-based complexes, paving the way for expanded investigations into their preparation, structural properties and potential utility in diverse fields.

Conflicts of interest

The authors declare that they have no known financial competitors or personal interests that could potentially influence the work reported in this paper.

Data availability

Data for this article are either included in the manuscript or are available from the corresponding authors upon request.

Supplementary information (SI): contains FT-IR spectra (Fig. S1–S5), NMR spectra (Fig. S6–S18), the molecular structure of **L** (Fig. S19), and views of intra- and intermolecular hydrogen bonds together with non-classical C–H···O interactions for all complexes (Fig. S20–S29). See DOI: https://doi.org/10.1039/d6ma00010j.

CCDC 2357130 (**L**), 2293084 (**1**), 2292951 (**3**), 2293085 (**4a**), 2293083 (**4b**) and 2292955 (**5**) contain the supplementary crystallographic data for this paper.[78a–f]

Acknowledgements

We gratefully acknowledge the funding support received for this project from Shahid Chamran University of Ahvaz (Grant number: SCU.SC1402.271). This research was also undertaken in part at the MX2 beamline at the Australian Synchrotron, part of ANSTO, Victoria, Australia, and made use of the Australian Cancer Research Foundation (ACRF) detector.

References

1 G. Mahmoudi, A. Bauzá and A. Frontera, *Inorg. Chim. Acta*, 2021, **516**, 120141.
2 F. A. Mautner, M. Scherzer, C. Berger, R. C. Fischer, R. Vicente and S. S. Massoud, *Polyhedron*, 2015, **85**, 20–26.
3 A. Escuer, J. Esteban and S. P. Perlepes, *Coord. Chem. Rev.*, 2022, **450**, 214245.
4 M. A. Goher, A. K. Hafez, M. A. Abu-Youssef, A. M. Badr, C. Gspan and F. A. Mautner, *Polyhedron*, 2004, **23**, 2349–2356.
5 A. Laachir, F. Rhoufal, S. Guesmi, E. M. Ketatni, L. Jouffret, N. Sergent, S. Obbade and F. Bentiss, *J. Mol. Struct.*, 2020, **1208**, 127892.
6 N. B. Nandi, S. Ghanta, J. Kłak, L. Sieroń, W. Maniukiewicz and T. K. Misra, *Polyhedron*, 2023, **230**, 116215.
7 A. Banerjee, S. Banerjee, C. J. Gómez García, S. Benmansour and S. Chattopadhyay, *ACS Omega*, 2019, **4**, 20634–20643.
8 A. Beheshti, K. Nozarian, E. S. Mousavifard, C. T. Abrahams, P. Mayer, R. Gajda, K. Woźniak and H. Motamedi, *J. Solid State Chem.*, 2021, **294**, 121874.
9 D. S. Yanick Gaelle, M. Ondoh Agwara, D. M. Yufanyi, J. Nenwa and R. Jagan, *Inorg. Nano-Met. Chem.*, 2017, **47**, 618–625.
10 D. S. Y. Gaëlle, D. M. Yufanyi, R. Jagan and M. O. Agwara, *Cogent Chem.*, 2016, **2**, 1253201.
11 J. D. Velasquez, J. Echeverría, C. F. Guerra and S. Alvarez, *Phys. Chem. Chem. Phys.*, 2024, **26**, 6683–6695.
12 A. Beheshti, A. Lalegani, G. Bruno, H. A. Rudbari and V. Nobakht, *Inorg. Chim. Acta*, 2013, **408**, 214–221.
13 A. Beheshti, V. Nobakht, L. Carlucci, D. M. Proserpio and C. Abrahams, *J. Mol. Struct.*, 2013, **1037**, 236–241.

14 S. S. Massoud, M. Dubin, A. E. Guilbeau, M. Spell, R. Vicente, P. Wilfling, R. C. Fischer and F. A. Mautner, *Polyhedron*, 2014, **78**, 135–140.
15 K. Fagnou and M. Lautens, *Angew. Chem., Int. Ed.*, 2002, **41**, 26–47.
16 E. Choi, N. Kwon, J. G. Kim, O. S. Jung and Y. A. Lee, *J. Mol. Struct.*, 2016, **1118**, 367–371.
17 D. A. Valyaev and Y. Canac, *Dalton Trans.*, 2021, **50**, 16434–16442.
18 A. Poddar and F. C. Pigge, *Organometallics*, 2024, **43**, 1608–1618.
19 S. Samiee, M. Bahmaiee, H. Motamedi, A. Shiralinia and R. W. Gable, *Polyhedron*, 2020, **74**, 114567.
20 S. J. Sabounchei and A. R. Dadrass, *Asian J. Chem.*, 2007, **7**, 5471–5476.
21 R. Visbal, N. Rosado, J. Zapata-Rivera and M. C. Gimeno, *Inorg. Chem.*, 2024, **63**, 6589–6599.
22 P. Laavanya, U. Venkatasubramanian, K. Panchanatheswaran and J. A. K. Bauerb, *Chem. Commun.*, 2001, 1660–1661.
23 N. A. Nesmeyanov, V. Novikov and O. Reutov, *J. Organomet. Chem.*, 1965, **4**, 202–210.
24 M. Kalyanasundari, K. Panchanatheswaran, W. T. Robinson and H. Wen, *J. Organomet. Chem.*, 1995, **491**, 103–109.
25 E. C. Spencer, M. B. Mariyatra, J. A. K. Howard, A. M. Kenwright and K. Panchanatheswaran, *J. Organomet. Chem.*, 2007, **692**, 1081–1086.
26 S. J. Sabounchei, H. Nemattalab, S. Salehzadeh, S. Khani, M. Bayat and H. R. Khavasi, *Polyhedron*, 2008, **27**, 2015–2021.
27 L. Vatannavaz, S. J. Sabounchei, A. Sedghi, M. Bayat, K. Van Hecke and A. Chehregani Rad, *J. Coord. Chem.*, 2020, **73**, 87–102.
28 C. R. Groom, I. J. Bruno, M. P. Lightfoot and S. C. Ward, *Acta Crystallogr., Sect. B: Struct. Sci., Cryst. Eng. Mater.*, 2016, **72**, 171–179.
29 E. I. Zhilyaeva, O. A. Bogdanova, R. N. Lyubovskaya, R. B. Lyubovskii, K. A. Lyssenko and M. Y. Antipin, *Synth. Met.*, 1999, **99**, 169–174.
30 E. C. Wang, J. Li, Y. L. Li, E. C. Yang and X. J. Zhao, *Synth. React. Inorg. Met.-Org. Chem.*, 2011, **41**, 791–797.
31 S. C. Jain and R. Rivest, *Inorg. Chim. Acta*, 1970, **4**, 291–295.
32 Z. Popović, G. Pavlović, D. M. Čalogović, Z. Soldin, M. Rajić, D. V. Topić and D. Kovaček, *Inorg. Chim. Acta*, 2000, **306**, 142–152.
33 Z. Bayat, A. Yousefi, S. J. Sabounchei, Z. Ahmadvand, M. Bayat, M. A. Khoei and R. W. Gable, *Sci. Rep.*, 2024, **14**, 20955.
34 D. Majumdar, A. Frontera, J. E. Philip, B. Gassoumi, S. Burguera, S. Roye and S. Ayachi, *RSC Adv.*, 2026, **16**, 332–352.
35 S. J. Sabounchei, M. Ahmadianpoor, A. Hashemi, F. Mohsenzadeh and R. W. Gable, *Inorg. Chim. Acta*, 2017, **458**, 77–83.
36 F. Maqsood, S. S. Al-Rawi, A. H. Ibrahim, F. Jamil, A. Zafar, M. A. Iqbal, U. S. Shoukat, M. Asad, S. Ullah, A. Farhan and M. Atif, *Rev. Inorg. Chem.*, 2025, **45**, 375–396.
37 I. O. Albert and R. N. Buncel, *Chem. Rev.*, 2004, **104**, 5911–5930.
38 J. Lemire, J. Harrison and R. Turner, *Nat. Rev. Microbiol.*, 2013, **11**, 371–384.
39 S. Bagger, B. R. Byberg and K. Breddamm, *J. Inorg. Biochem.*, 1991, **42**, 97–103.
40 T. W. Clarkson and L. Magos, *Crit. Rev. Toxicol.*, 2006, **36**, 609–662.
41 B. Kang, J. Wang, S. Guo and L. Yang, *Total Environ.*, 2024, **943**, 173577.
42 P. L. Lam, G. L. Lu, K. H. Choi, Z. Lin, S. H. L. Kok, K. K. H. Lee, K. H. Lam, H. Li, R. Gambari, Z. X. Bian, W. Y. Wong and C. H. Chui, *RSC Adv.*, 2016, **6**, 16736–16744.
43 S. Samiee, H. Rashedi, V. Nobakht, H. Motamedi and R. W. Gable, *J. Mol. Struct.*, 2025, **1336**, 142104.
44 *Mercury 3.0*, Cambridge Crystallographic Data Centre, Cambridge, 2018.
45 V. A. Blatov, A. P. Shevchenko and D. M. Proserpio, *Cryst. Growth Des.*, 2014, **14**, 3576–3586.
46 *CrysAlisPro Software system, version 1.171.42.94a*, Rigaku Oxford Diffraction, Rigaku Corporation, Wroclaw, Poland, 2023.
47 D. Aragão, J. Aishima, H. Cherukuvada, R. Clarken, M. Clift, N. P. Cowieson, D. J. Ericsson, C. L. Gee, S. Macedo and N. Mudie, *J. Synchrotron Radiat.*, 2018, **25**, 885–891.
48 W. Kabsch, *Acta Crystallogr., Sect. D: Biol. Crystallogr.*, 2010, **66**, 125–132.
49 G. M. Sheldrick, *SADABS*, Bruker AXS Inc., Madison, WI, 2002.
50 O. Dolomanov, L. Bourhis, R. Gildea, J. Howard and H. Puschmann, *J. Appl. Crystallogr.*, 2009, **42**, 339–341.
51 G. M. Sheldrick, *Acta Crystallogr., Sect. A: Found. Adv.*, 2015, **71**, 3–8.
52 G. M. Sheldrick, *Acta Crystallogr., Sect. C: Struct. Chem.*, 2015, **71**, 3–8.
53 R. G. Pearson, *J. Am. Chem. Soc.*, 1963, **85**, 3533.
54 R. G. Pearson, *J. Chem. Educ.*, 1968, 581.
55 R. G. Pearson, *Chemical Hardness – Applications From Molecules to Solids*, Wiley-VCH, Weinheim, 1997, p. 198.
56 N. A. Bell, T. N. Branston, W. Clegg, L. Parker, E. S. Raper, C. Sammon and C. P. Constable, *Inorg. Chim. Acta*, 2001, **319**, 130.
57 O. Kazuhiko, T. Toshiyuki, I. Shin-ichi and O. Hitoshi, *Bull. Chem. Soc. Jpn.*, 1989, **62**, 1875.
58 A. E. Martell, *Adv. Chem.*, 1967, **62**, 272.
59 S. J. Sabounchei, A. Dadrass, M. Jafarzadeh and H. R. Khavasi, *Acta Crystallogr., Sect. E: Struct. Rep. Online*, 2007, **63**, o3160.
60 S. J. Sabounchei, H. Nemattalab and H. R. Khavasi, *X-Ray Struct. Anal. Online*, 2010, **26**, 35–36.
61 J. E. Huheey, *Inorg. Chem.*, Harper & Row, New York, 3rd edn, 1983.
62 M. Llunell, D. Casanova, J. Cirera, P. Alemany and S. Alvarez, *SHAPE, Version 2.1*, Universitat de Barcelona, Barcelona, Spain, 2013.
63 S. Alvarez, P. Alemany, D. Casanova, J. Cirera, M. Llunell and D. Avnir, *Coord. Chem. Rev.*, 2005, **249**, 1693–1708.

64 S. J. Sabounchei, H. Nemattalab, S. Salehzadeh, M. Bayat, H. R. Khavasi and H. Adams, *J. Organomet. Chem.*, 2008, **693**, 1975–1985.
65 M. Akkurt, K. Karami, Ş. P. Yalçın and O. Büyükgüngör, *Acta Crystallogr., Sect. E: Struct. Rep. Online*, 2008, **64**, m612–m613.
66 W. Li, E. Rose, M. V. Tran, R. Hübner, A. Łapiński, R. Świetlik, S. A. Torunova, E. I. Zhilyaeva, R. N. Lyubovskaya and M. Dressel, *J. Chem. Phys.*, 2017, **147**, 064702.
67 D. Naumann, F. Schulz, I. Pantenburg and W. Tyrra, *Z. Anorg. Allg. Chem.*, 2004, **630**, 529–534.
68 I. Tikhonova, F. Dolgushin, A. Yanovsky, Y. T. Struchkov, A. Gavrilova, L. Saitkulova, E. Shubina, L. Epstein, G. Furin and V. Shur, *J. Organomet. Chem.*, 1996, **508**, 271–273.
69 M. Bahrani-Pour, A. Beheshti, T. Sedaghat, E. Hoveizi, N. Naseri, P. Mayer and R. Centore, *Dalton Trans.*, 2023, **52**, 683–695.
70 A. Schulz and A. Villinger, *Chem. – Eur. J.*, 2015, **21**, 3649.
71 T. S. B. Baul, S. Kundu, H. Hopfl, E. R. T. Tiekink and A. Linden, *J. Coord. Chem.*, 2014, **67**, 1061.
72 B. H. Kim and G. M. Gadd, *Prokaryotic Metabolism and Physiology*, Cambridge University Press, Cambridge, 2nd edn, 2019.
73 N. Molchanova, J. E. Nielsen, K. B. Sørensen, B. K. Prabhala, P. R. Hansen, R. Lund, A. E. Barron and H. Jenssen, *Sci. Rep.*, 2020, **10**, 14807.
74 M. T. Madigan, K. S. Bender, D. H. Buckley, W. M. Sattley and D. A. Stahl, *Brock Biology of Microorganism*, Pearson Education, Malaysia, 15th edn, 2019, pp. 70–104.
75 L. F. Múnera-Gómez, L. Fernanda, J. C. Muñoz-Acevedo and E. Pabón-Gelves, *Revista DYNA*, 2024, **91**, 16–23.
76 R. G. Karki and V. M. Kulkarni, *Bioorg. Med. Chem.*, 2001, **9**, 3153–3160.
77 N. Kumar, R. Kaushal and P. Awasthi, *J. Fluoresc.*, 2025, **35**, 10445–10461.
78 (*a*) CCDC 2357130: Experimental Crystal Structure Determination, 2026, DOI: 10.5517/ccdc.csd.cc2mg75j; (*b*) CCDC 2293084: Experimental Crystal Structure Determination, 2026, DOI: 10.5517/ccdc.csd.cc2mg75j; (*c*) CCDC 2292951: Experimental Crystal Structure Determination, 2026, DOI: 10.5517/ccdc.csd.cc2mg75j; (*d*) CCDC 2293085: Experimental Crystal Structure Determination, 2026, DOI: 10.5517/ccdc.csd.cc2mg75j; (*e*) CCDC 2293083: Experimental Crystal Structure Determination, 2026, DOI: 10.5517/ccdc.csd.cc2mg75j; (*f*) CCDC 2292955: Experimental Crystal Structure Determination, 2026, DOI: 10.5517/ccdc.csd.cc2mg75j.